Model-Based Weather Radar Remote Sensing of Explosive Volcanic Ash Eruption

Frank Silvio Marzano, *Senior Member, IEEE*, Sara Marchiotto, Christiane Textor, and David J. Schneider

***Abstract*—Microphysical and dynamical features of volcanic ash clouds can be quantitatively monitored by using ground-based microwave weather radars. These systems can provide data for determining the ash volume, total mass, and height of eruption clouds. In order to demonstrate the unique potential of this microwave active remote-sensing technique, the case study of the eruption of Augustine Volcano in Alaska in January 2006 is described and analyzed. Volume scan data, acquired by a NEXRAD WSR-88D S-band ground-based weather radar, are processed to automatically classify and estimate eruptive cloud particle concentration. The numerical results of the coupled model Z-reflectivity from Active Tracer High resolution Atmospheric Model (ATHAM), including particle aggregation processes and simulation of radar reflectivity from the ATHAM microphysical model, are exploited to train the inversion algorithm. The volcanic ash radar retrieval based on the ATHAM algorithm is a physical-statistical approach based on the backscattering microphysical model of volcanic cloud particles (hydrometeors, ash, and aggregates), used within a Bayesian classification and optimal regression algorithm. A sensitivity analysis is carried out to evaluate the overall error budget. The evolution of the Augustine eruption is discussed in terms of radar measurements and products, pointing out the unique features, the current limitations, and future improvements of radar remote sensing of volcanic plumes.**

***Index Terms*—Ash particle aggregation, ash retrieval, inversion methods, microwave radars, numerical simulation, volcanic eruption clouds.**

I. Introduction

VOLCANIC ash is a natural hazard whose effects have been well documented. Volcanic ash is a significant hazard to aircraft operations (e.g., see [1] and [2]), and the threat to public safety posed by volcanic ashfall at the surface is significant as well (e.g., see [3]–[5]). Given the significance of the hazards posed by volcanic ash, timely detection and tracking of the ash plume is essential to a successful warning process, particularly during and immediately following an eruptive event.

A variety of satellite techniques have been successfully used to track volcanic ash clouds; however, these techniques have certain limitations [6]–[8]. These data are subject to limitations in both spatial and temporal resolution. Issues involving the detection of ash clouds using infrared brightness temperature differencing, a commonly used method, have been addressed, suggesting several scenarios where effective infrared satellite detection of volcanic ash clouds may be compromised [9], [10]. The brightness temperature differencing, also known as the "split-window" method, was shown to be subject to errors when the volcanic plume lies over a very cold surface or when the plume lies above a clear land surface at night where strong surface temperature and moisture inversions exist [10]. These scenarios can often be found over cold regions such as Alaska, particularly in the winter. In addition, the availability of visible satellite data is often severely restricted in the winter due to the limited amount of daylight.

Ground-based microwave radar systems can have a valuable role in volcanic ash cloud monitoring as evidenced by available radar imagery (e.g., see [11] and [12]). These systems represent one of the best methods for real-time and areal monitoring of volcano eruption, in terms of its intensity and dynamics. The possibility of monitoring 24 h a day, in all weather conditions, at a fairly high spatial resolution (less than a few hundreds of meters), and in every few minutes after and during the eruption is the major advantage of using ground-based microwave radar systems. They can provide data for determining the ash volume, total mass, and height of eruption clouds [1], [11], [12].

There are still several open issues about microwave weather radar capabilities to detect and quantitatively retrieve ash cloud parameters [13]. A major impairment in the exploitation of microwave weather radars for volcanic eruption monitoring is due to the exclusive use of operational weather radars for clouds and precipitation observation. Several unknowns may also condition the accuracy of radar products, where most of them are related to microphysical variability of ash clouds due to particle size distribution (PSD), shape, and dielectric composition. Some of them were analyzed in a previous work where the sensitivity of microwave radar response to particle ash distribution and wavelength was investigated using *ad-hoc* physically oriented random schemes of eruptive ash cloud volumes [14]. Fine-size ash, medium-size ash, and lapilli were distinguished, with mean diameters of about 0.01, 0.1, and 1 mm, respectively, and concentrations of up to few tens of grams per cubic meter. The electromagnetic behavior of pure

Manuscript received July 10, 2009; revised November 21, 2009 and March 6, 2010. Date of publication June 14, 2010; date of current version September 24, 2010. This work was supported in part by the Italian Department of Civil Protection, Rome, Italy, by the Sapienza University of Rome, Rome, Italy, and by the U.S. Department of Commerce under Grant BS123456.

F. S. Marzano and S. Marchiotto are with the Department of Electronic Engineering, Sapienza University of Rome, 00184 Rome, Italy, and also with the Center of Excellence CETEMPS, University of L'Aquila, 67010 L'Aquila, Italy (e-mail: marzano@die.uniroma1.it).

C. Textor is with the Deutsche IPCC-Koordinierungsstelle–Projektträger im DLR Umwelt, Kultur, Nachhaltigkeit Heinrich-Konen-Str.1–53227 Bonn, Germany (e-mail: christiane.textor@dlr.de).

D. J. Schneider is with the U.S. Geological Survey—Alaska Volcano Observatory, Alaska Science Center, Anchorage, AK 99508 USA (e-mail: djschneider@usgs.gov).

Color versions of one or more of the figures in this paper are available online at http://ieeexplore.ieee.org.

Digital Object Identifier 10.1109/TGRS.2010.2047862

0196-2892/$26.00 © 2010 IEEE

and porous ash particles was also modeled, and its impact on radar reflectivity signature was analyzed for fine ash, medium ash, and lapilli. No particle aggregation mechanisms and effects were considered in these works.

Indeed, the aggregation of volcanic ash particles within the eruption column of explosive eruptions has been observed at many volcanoes [11]. Recent satellite observations of ash clouds provide strong indirect evidence that ice may be present on ash particles [15]–[18]. The aggregation influences the residence time of ash in the atmosphere and the radiative properties of the "umbrella" cloud (i.e., ash at the height of neutral buoyancy (HNB) spreading in the horizontal and vertical directions). Numerical experiments are helpful in exploring the processes occurring in the eruption column. Some advanced plume models can simulate the interactions of hydrometeors and volcanic ash, including aggregate particle formation within a rising eruption column (e.g., see [19] and [20]).

This paper attempts to illustrate the potential of radar data in observing volcanic ash clouds, using a case study dealing with an Alaska volcanic eruption in 2006 [1]. This event was the first time that a significant volcanic eruption was fully observed within the nominal range of WSR-88D (which stands for Weather Surveillance Radar, 1988, Doppler) S-band radar system. Radar data, in conjunction with pilot reports, proved to be crucial in analyzing the height and movement of volcanic ash clouds during and immediately following each eruptive event. This data greatly aided National Weather Service meteorologists in the issuance of timely and accurate warning and advisory products to aviation, public, and marine interests.

The objective of this paper is to design a physically based ash retrieval algorithm. To this aim, an advanced plume numerical model, named as Active Tracer High resolution Atmospheric Model (ATHAM), is used to investigate processes leading to particle aggregation in the eruption column [19]–[21]. A microwave radar reflectivity model, coupled with ATHAM and then named Z-ATHAM (i.e., ATHAM with the module of radar reflectivity Z), is also developed to analyze the sensitivity of microwave radar response to the aggregation of ash particles and hydrometeors.

This paper is organized as follows. In Section II, the relationship between radar reflectivity factor and ash aggregate concentration is derived for the various particle classes by applying a radar reflectivity microphysical model, developed from results of numerical experiments performed with Z-ATHAM. The ash retrieval physical-statistical algorithm is based on the backscattering microphysical model of volcanic cloud particles, used within a Bayesian classification and optimal regression algorithm. In Section III, a case study on the eruption of Augustine Volcano in January 2006 is described and analyzed. Finally, the retrieval procedure is applied to WSR-88D S-band radar data that are available during the eruption of the Augustine Volcano on January 13, 2006, in Section IV. The evolution of the Augustine vulcanian eruption is discussed in terms of radar measurements, and examples of the achievable retrieval algorithm products are presented and discussed. Finally, the conclusion in Section V discusses the unique features, the current limitations, and future improvements of radar remote sensing of volcanic plumes. The Appendices provide some details about the ATHAM plume model and radar echo simulations.

II. Physically Based Inversion Methodology

The interpretation of measured radar reflectivity in terms of useful geophysical parameters can be posed as an inverse problem. In order to circumvent the nonuniqueness and instability of the inverse solution, the problem can be stated in a probabilistic framework. A crucial role is played by the *a priori* geophysical information, which represents a constraint within the inverse problem. In our context, this means to construct an effective model of ash cloud microphysics for remote-sensing purposes.

The ash retrieval algorithm is physically based as it couples a backscattering microphysical model of volcanic particle ensemble with a regressive estimation. The relationships between radar reflectivity factor and mass particle concentration within the volcanic cloud have been derived for the four particle classes by applying the radar reflectivity microphysical model Z-ATHAM. As discussed in Appendices A and B, we have generated the training data set with the Z-ATHAM simulation named EXP3, characterized by relatively large initial size modes, extracting data from 30-, 60-, and 90-min simulation times. This simulated data set may be considered as a physically consistent extension of the randomly generated data set, illustrated in a previous study. The obvious advantage of the current approach is that a robust microphysical basis can be provided to the simulated ash volume samples. The Plinian eruption mode study ensures, on the other hand, a large variety of environmental conditions and volcanic processes in terms of temperature, mixture, and particle concentration.

Four particle classes x were considered in ATHAM, defined by size categories and hydrometeor types depending on the local temperature, as thoroughly discussed in Appendix A: 1) "small warm" particle, i.e., possible aggregation of cloud water and small ash particles at $T > T_0$ (with T_0 as the freezing temperature); 2) "small cold" particle, i.e., possible aggregation of cloud ice and small ash particles at $T < T_0$; 3) "large warm" particle, i.e., possible aggregation of rain and large ash particles at $T > T_0$; and 4) "large cold" particle, i.e., possible aggregation of graupel and large ash particles at $T < T_0$.

Fig. 1 shows the four particle classes simulated in the ATHAM simulation EXP3, in terms of particle mass concentration C_{px} (see Appendix B for details) versus synthetic measured reflectivity Z_{Hm}. The synthetic measured reflectivity factor Z_{Hm} has been obtained from Z_H, computed using the Mie theory, by introducing a zero-mean Gaussian random error ε_Z with a given variance $\sigma^2_{\varepsilon Z}$ [12]. The error sources may be ascribed to instrumental noise (about 1-dBZ variance) and to modeling uncertainties (about 1-dBZ variance). If the error sources are statistically independent, the overall error standard deviation of Z_{Hm} can be assumed to be equal to about $\sqrt{1+1} = 1.4$ dBZ. Fig. 1 suggests that the four particle classes are quite well discriminated in terms of Z_{Hm}, and a linear curve between C_{px} and Z_{Hm} in a logarithmic plane may model their functional relation. The large dynamics of both C_{px} and Z_{Hm} is noted with values of up to 10^3 g/m^3 and 100 dBZ,

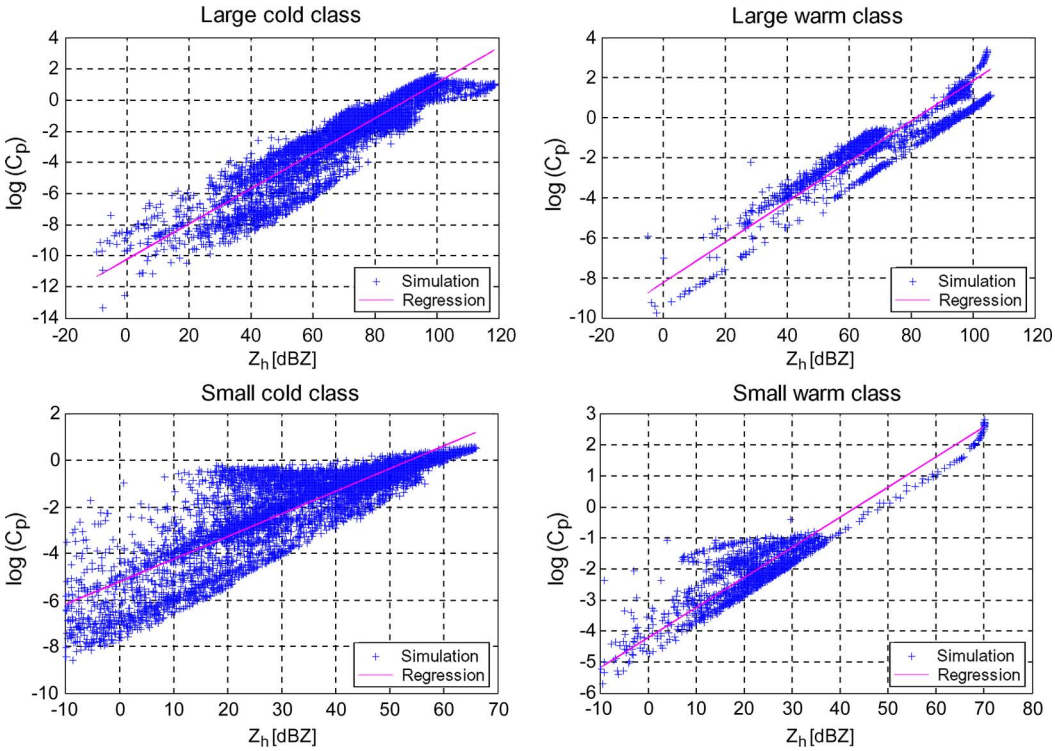

Fig. 1. Correlation diagram between particle concentration C_{px} and synthetic measured ash reflectivity Z_{Hm} at S-band for each volcanic cloud particle class (i.e., large cold, large warm, small cold, and small warm classes), derived from Z-ATHAM model simulations. The continuous lines represents the regression curve in the considered logarithmic plane $C_{px}-Z_{Hm}$.

respectively, for large-size classes covering both sub-Plinian and Plinian eruption scenarios. Larger values are typical of Plinian eruptions with on-going aggregation processes.

In order to quantitatively evaluate the ash retrieval by weather radars, we follow the same procedure proposed in [12]. Starting from the Z-ATHAM model characterization of volcanic cloud reflectivity and from given radar specifications, the physically based volcanic cloud radar retrieval algorithm has been employed in the following two cascade steps: 1) detection of the particle class from the measured reflectivity Z_{Hm} and the altitude h characterizing every range bin by using a Bayesian identification technique and 2) estimation of the eruptive material amount from the measured Z_{Hm} by applying a parametric regression method.

Fig. 2 shows the overall scheme of the *Volcanic Ash Radar Retrieval using ATHAM* (VARR-A) methodology for ground-based microwave weather radars. After a preliminary phase to elaborate the *a priori* information about the environmental conditions in the area of the eruption event, the classification and the estimation stages of the algorithm are introduced.

Within the preliminary stage, the measured Z_{Hm} and the height of each range bin h are used to determine the freezing level height h_{FL}, which is crucial for the classification process in order to correctly detect warm and cold categories. Vertical profiles of temperature can be derived from local atmospheric radiosoundings, meteorological forecasts, or climatological models. Ancillary information about cloud and rain patterns, together with atmospheric water vapor field, may support the decision about the presence of hydrometeors and aggregation processes within the volcanic area. Satellite data from radiometric sensors aboard satellites can be employed to retrieve columnar water vapor content and cloud, and rain patterns.

The following two cascade steps in Fig. 2 are trained by the Z-ATHAM microphysical radar model, parameterized by microwave radar specifications (observation angles, operational frequency, and signal-to-noise ratio). In the following sections, we will describe the overall retrieval procedure, analyzing separately the two retrieval cascade steps. A sensitivity analysis is carried out to evaluate the expected error budget using S-band radar simulated data.

A. Estimation and Classification

The classification step is an attempt to automatically discriminate between particle categories of large/small and warm/cold type. In the overall retrieval scheme, classification may represent a first qualitative output before performing parameter estimation. A radar resolution volume (defined by the pulse duration and transverse section of the antenna beamwidth) can be characterized by the measured radar reflectivity factor and possible meteorological observables as local temperature T or, alternatively, the freezing-level height h_{FL} [above sea level (asl)]. Within the Bayesian theory, assigning the correct volcanic particle class to radar bins implies the knowledge of *a posteriori* conditional probability density functions (pdfs) $p(x|Z_{Hm})$, where x is the unknown particle class. The maximum *a posteriori* probability (MAP) decision rule is quite intuitive, as the particle class is provided by the index x that maximizes the conditional posterior pdfs. The MAP criterion

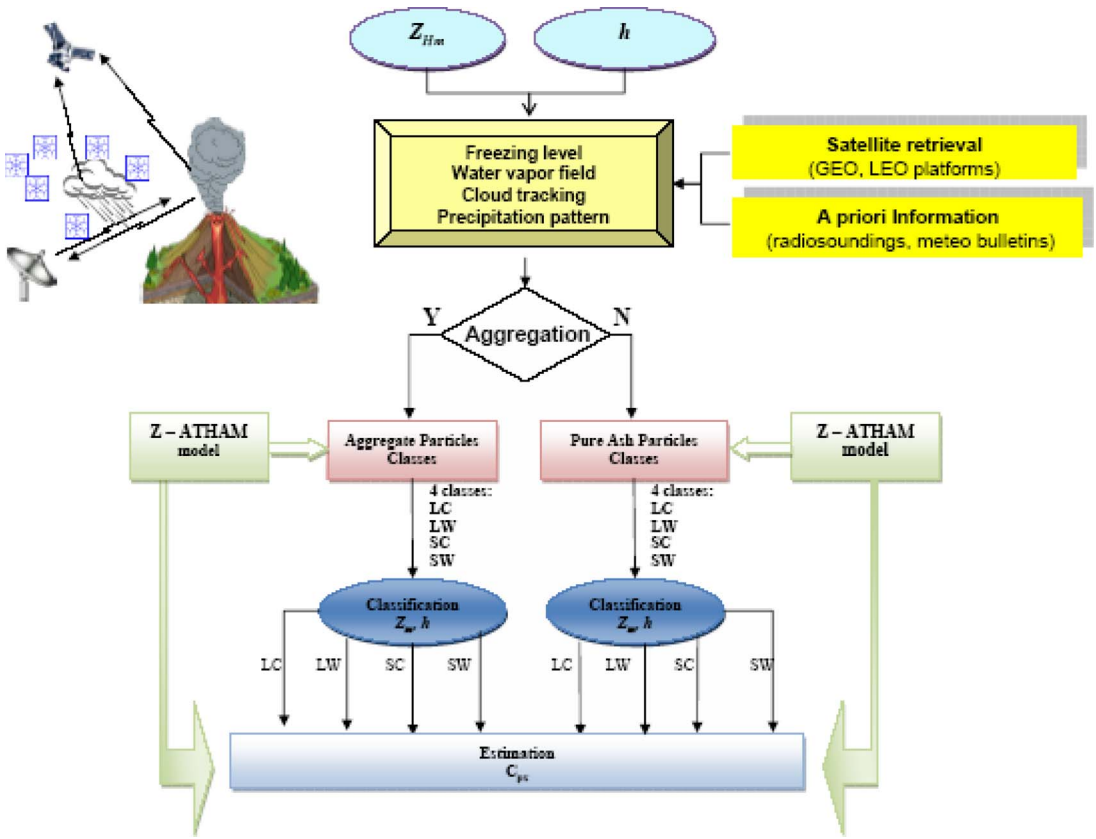

Fig. 2. Schematic block diagram of the VARR-A algorithm for ground-based microwave weather radars. After a preliminary phase to elaborate the *a priori* information about the environmental conditions, the classification and the estimation stages of the retrieval algorithm are depicted. The class labels are the following: large cold (LC), large warm (LW), small cold (SC), and small warm (SW). The variables Z_{Hm} and h indicate the measured reflectivity factor and range bin altitude, respectively. Z-ATHAM stands for the coupled reflectivity-ATHAM model.

can be used to carry out cloud classification in a model-based supervised context [13], [24].

The MAP approach is framed within the general Bayesian theory, and it offers the advantage to insert, in a rigorous manner, both the forward modeling and *a priori* information [13]. Using the Bayes theorem, if x is the ash class, then the conditional pdf of a class x given a measurement Z_{Hm} can be expressed as

$$p(x|Z_{Hm}) = \frac{p(Z_{Hm}|x)p(x)}{p(Z_{Hm})} \cong \frac{p(\Delta Z_x)p(x)}{p(Z_{Hm})} \qquad (1)$$

where $\Delta Z_x = Z_{Hm} - m_{Zx}$ (in decibels and referenced to zero) is the perturbation of the reflectivity measurements from the reflectivity mean value (centroid) m_{Zx} of class x and $p(x)$ represents the *a priori* discrete pdf of class x. If $p[\Delta Z_x]$ is assumed to be a Gaussian pdf, the MAP estimation of ash class x corresponds to the following maximization with respect to x:

$$\hat{x} = \mathrm{Max}_x \left[-\frac{(Z_{Hm} - m_{Zx})^2}{\sigma_{Zx}^2} + \ln \sigma_{Zx}^2 - 2 \ln p(x) \right] \qquad (2)$$

where Max_x is an operator returning the value of x corresponding to its argument maximum and σ_{Zx} (in decibels and referenced to zero) is the reflectivity standard deviation of class x, whereas the ash class perturbations have been assumed uncorrelated.

Computing (2) requires knowledge of the reflectivity mean m_{Zx} and standard deviation σ_{Zx} of each ash class x. This statistical characterization of each cloud class can be derived either from measured data, if available, or from a simulated data set, as we have done here, by means of the Z-ATHAM numerical model. From Fig. 1, it is possible to deduce both the mean m_{Zx} and variance σ_{Zx}^2 for four-class discrimination.

The *a priori* probability $p(x)$ can be used to subjectively weigh each class as a function of other available information (such as coincident satellite and/or *in situ* data). Through this prior pdf, we can impose, for example, the existence of a class conditioned to radar measurements and environmental conditions [24]. Due to lack of further information, we have simply exploited the altitude, which provides a rough information about temperature, to suppress some particle classes that, we believe, cannot exist outside a given altitude range. This means that the prior pdf can be approximated as

$$p(x) = p(x|h, \Delta h = h - h_0) = P_x(\Delta h) \qquad (3)$$

where Δh is the altitude range, h_0 is the freezing level, and P_x is the discrete probability of class c, depending on Δh. Note that $\Sigma_x P_x(\Delta h) = 1$ holds. Typical altitudes of each particle class and their associated probabilities are shown in Table I.

A simple test of the MAP classification procedure is represented by the results expressed by the contingency matrix where, for each input class, the number of correct and incorrect

TABLE I
ALTITUDE RANGES AND CORRESPONDING SUPPRESSED PARTICLE CLASSES. SUPPRESSION IS CARRIED OUT BY PREDEFINED SETS OF *A PRIORI* PROBABILITIES

Δh	*p(x) Large cold class*	*p(x) Large warm class*	*p(x) Small cold class*	*p(x) Small warm class*
$\Delta h>0$	0.5	0	0.5	0
$\Delta h<0$	0	0.5	0	0.5

TABLE II
CONTINGENCY ERROR TABLE, EXPRESSED IN PERCENTAGE, FOR THE FOUR PARTICLE CLASSES

MAP (Z_{Hm}, h)	Large cold class	Large warm class	Small cold class	Small warm class
Large cold class	93.83	0	6.17	0
Large warm class	0	63.97	0	36.03
Small cold class	1.83	0	98.16	0
Small warm class	0	0.72	0	99.28

classifications is counted. Table II reports the contingency error table expressed in percentage. Note that the sum of percentages along a row is always, by construction, equal to 100%, whereas the input classes are those listed along the rows. The classification error budget indicates that cold and warm categories are always well distinguished, whereas it is not the same for large and small warm categories that partially overlap each other.

Once a particle class is detected, then an estimate of particle concentration is possible. A way to approach the quantitative retrieval problem is to adopt a statistical parametric model to describe the relation $C_{px}-Z_{Hm}$ [12]. Assuming a power-law model, we can write the estimated concentration for each class c as

$$\hat{C}_{px} = a_x[Z_{H_m}]^{b_x} \tag{4}$$

where $x = 1:4$, the "hat" indicates an estimated quantity with a_x, and b_x is the regression coefficients. For the four particle classes, Table III shows the mean percentage error (MPE), the root mean square error (rmse), and correlation coefficient ρ, which are defined for C_{px} as

$$\begin{cases} MPE = 100 \cdot \sum_{i=1}^{N} \left(\frac{\hat{C}_{px}(i) - C_{px}(i)}{C_{px}(i)} \right) \frac{1}{N} \\ rmse = 100 \cdot \sum_{i=1}^{N} \left[\hat{C}_{px}(i) - C_{px}(i) \right]^2 \frac{1}{N} \\ \rho(C_{px}, \hat{C}_{px}) = \frac{\mathrm{Cov}(C_{px}, \hat{C}_{px})}{\sigma(C_{px})\sigma(\hat{C}_{px})}. \end{cases} \tag{5}$$

where N is the number of data available, Cov indicates the covariance between the two quantity, and σ is the standard deviation. The optimal values of these statistical indexes MPE, rmse, and ρ are 0, 0, and 1, respectively.

In order to reduce the impact of the ATHAM data set outliers (see Fig. 1), we have considered only the simulated samples of each class within the 90% of their probability density. The estimation error budget, shown in Table III, indicates a problem of overestimation for the small-size categories and of underestimation for the large-size categories, especially for the small warm class. The rmse is large for the warm categories. Anyway, for all classes, a fairly high degree of correlation is obtained, which indicates a good degree of accuracy in the estimation method.

TABLE III
ERROR BUDGET OF THE RETRIEVAL ALGORITHM FOR PARTICLE CONCENTRATION ESTIMATION IN TERMS OF MPE AND CORRELATION COEFFICIENT FOR EACH PARTICLE CLASS

Estimation C_p-Z_{Hm}	Large cold class	Large warm class	Small cold class	Small warm class
RMSE (g/m^3)	3.73	11.35	1.33	16.72
MPE **(%)**	-28.90	-35.80	11.48	-2.59
$\rho(C_p, \hat{C}_p)$	0.81	0.93	0.81	0.99

III. ALASKA CASE STUDY

The sub-Plinian eruption of the Augustine Volcano during the period January 11–28, 2006, presented a variety of challenges and opportunities for forecasters, scientists, and emergency managers throughout South-central Alaska. This event was observed by the Next-Generation Radar (NEXRAD) WSR-88D radar located in Kenai, Alaska [1].

A. Augustine Volcano Eruption in January 2006

The Augustine Volcano is 1260 m high (4134 ft) and is a conically shaped island stratovolcano located in southern Cook Inlet, about 290 km (180 mi) southwest of Anchorage, Alaska. The Augustine Volcano, shown in Fig. 3, is the most active volcano in the Cook Inlet region, with five significant eruptions (1883, 1935, 1963–64, 1976, and 1986) prior to 2006. These eruptions were primarily explosive events that produced volcanic ash clouds at their onset, followed by the emplacement of summit lava domes or flows. The explosive phase of the 2006 eruption consisted of thirteen discrete vulcanian explosions from January 11 to 28, with seismic durations that ranged from 1 to 11 min. These violent explosive events are characterized by the ballistic ejection of volcanic blocks and bombs and the emission of volcanic ash, and they were accompanied by atmospheric pressure waves [25]. Cloud heights during this phase varied from 7.5- to 14-km asl. The character of the eruption changed to a more continuous ash emission phase from January 28 to February 2, which produced ash plumes at lower altitudes (below 4-km asl).

The ability of the NEXRAD radar to provide near-real-time updates on the position and altitude of volcanic ash clouds was vital in providing timely and accurate forecasts and warnings [1]. One of the most significant contributions made by the radar data was in short-term aviation forecasting. Radar cross-sections were routinely used in diagnosing the vertical disposition of ash clouds during each event. These observations, in tandem with pilot reports, were used to ascertain the vertical extent of the ash clouds and to issue timely advisories to the aviation community [25]. The ability to track the volcanic ash in the short term was also vital to issuing timely and location-specific volcanic ashfall advisories. The ability to monitor the

Fig. 3. Photograph of the Augustine Volcano (with the vent peak at 1260 m) during an eruption, as seen from the east.

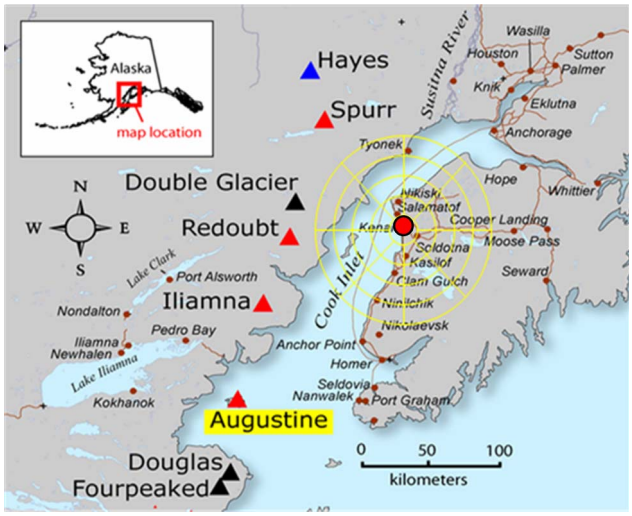

Fig. 4. Location of the Kenai NEXRAD WSR-88D radar (filled circle), located on the western Kenai Peninsula, approximately 190 km northeast of Augustine Volcano, and located in southern Cook Inlet, about 290 km southwest of Anchorage, Alaska.

movement of the volcanic ash cloud on a minute-by-minute basis was essential, given the close proximity of Augustine to settlements around the Cook Inlet region. In addition, marine weather statements were issued, alerting mariners to the potential hazards posed by the volcanic ash [1].

B. NEXRAD WSR-88D Radar Characteristics

The Kenai NEXRAD WSR-88D is an S-band radar with a Doppler capability. The radar site is located on the western Kenai Peninsula, approximately 190 km northeast of Augustine Volcano, as shown in Fig. 4. Table IV resumes operational selected characteristics for the Kenai S-band radar system.

NEXRAD is a network of 158 high-resolution Doppler weather radars, deployed throughout the U.S. and at selected overseas locations and operated by the National Weather Service, an agency of the National Oceanic and Atmospheric Administration within the U.S. Department of Commerce. The technical name of the radar system is WSR-88D. NEXRAD

TABLE IV
TECHNICAL CHARACTERISTIC OF KENAI NEXRAD WSR-88D RADAR

TRANSMITTER	
Frequency	S-band (2700-3000 MHz)
Klystron power peak	750 kW
Pulse repetition frequency	318-1304 Hz
ANTENNA	
Paraboloid type	Center-fed with 28 ft. diameter
Polarization	Linear horizontal
Main-lobe beam-width	0.925 (at 2850 MHz)
Rodome	Semi-sphere with 39 ft. diameter
Antenna gain	45 dBi
Minimum detectable signal	-113 dBm
PROCESSOR	
Range increment	250 m
Azimuth increment	1 degree
PRODUCTS	
Level II	Reflectivity, velocity, spectrum width
Level III	Reflectivity, velocity (Alaska site)

detects precipitation and atmospheric wind. It returns data which when processed can be displayed in a *mosaic* map which shows patterns of precipitation and its movement.

The major difficulty in using an operational system, such as WSR-88D, to monitor a volcanic eruption is that its daily schedule is necessarily devoted to meteorological targets. In our case, the radar system operates in two basic modes that are selectable by the operator: a slow-scanning *clear-air mode* for analyzing air movements when there is little or no activity in the area and a *precipitation mode* with a faster scan time for tracking active weather.

Unlike the majority of WSR-88D radars in the network, Alaska radars are owned and maintained by the Federal Aviation Administration. The radar system provides two types of radar products: the data level II types and the data level III types. The level III data, as described in [26], are generated from the radar product generator (RPG) (that is where the algorithms compute all of the derived fields). These consist of the actual base products, e.g., base reflectivity, base velocity, and spectrum width, in addition to a selection of derived products including echo tops and vertically integrated liquid (VIL). However, there are limits on the temporal availability of certain products. For example, composite reflectivity is available only every third volume scan at Level III, while base reflectivity is available every volume scan. Level II data allow for a wider array of products to be derived, whereas with Level III data, the user is limited to the archived product database. Unfortunately, Level II data were not available from Alaska WSR-88D platforms at this time. In this paper, the base reflectivity data of the NEXRAD Level III data from the Kenai radar site were collected and used. The resolution of the reflectivity data is 1° in azimuth and an elevation angle of 1 km in range resolution.

During the January 2006 Augustine eruption, the WSR-88D radar at Kenai operated in a variety of scanning modes or volume coverage patterns (VCPs). VCPs 12, 21, 31, and 32 were the scanning modes employed during the course of the eruption. The specifications of each scanning mode are displayed in Table V. Table VI shows the scanning strategy that was employed for each of the 13 events during the eruption.

TABLE V
NEXRAD VOLUME COVERAGE PATTERN SPECIFICATIONS

Volume Coverage Pattern	Radar Mode (Sensitivity)	Elevation Angles (Degrees)	Pulse Length (μs)	Scan Duration (Minutes)
12	Precipitation Low Sensitivity	0.5, 0.9, 1.3, 1.8, 2.4, 3.1, 4.0, 5.1, 6.4, 8.0, 10.0, 12.5, 15.6, 19.5	1.57	4.1
21	Precipitation Low Sensitivity	0.5, 1.5, 2.4, 3.4, 4.3, 6.0, 9.0, 14.6, 19.5	1.57	6
31	Clear Air High Sensitivity	0.5, 1.5, 2.5, 3.5, 4.5	4.70	10
32	Clear Air High Sensitivity	0.5, 1.5, 2.5, 3.5, 4.5	1.57	10

TABLE VI
EXPLOSIVE EVENTS AND MODE OF OPERATION FOR KENAI NEXRAD

Explosive Event	Start Date and Time (UTC)	VCP	Mode
1	1/11/2006 13:44	12	Precip
2	1/11/2006 14:12	12	Precip
3	1/13/2006 13:24	12	Precip
4	1/13/2006: 17:47	12	Precip
5	1/13/2006: 20:22	31	Clear Air
6	1/14/2006: 01:40	31	Clear Air
7	1/14/2006: 03:38	31	Clear Air
8	1/14/2006: 09:14	21	Precip
9	1/17/2006: 16:58	21/32	Both
10	1/28/2006: 05:24	31	Clear Air
11	1/28/2006: 08:37	31	Clear Air
12	1/28/2006: 11:04	31	Clear Air
13	1/28/2006: 16:42	31	Clear Air

During several eruption events, the Kenai radar employed the scanning mode VCP 12. Fig. 5 shows the altitude of the radar beam above the Augustine Volcano. One of the strengths of VCP 12 is the number of elevation scans at lower angles, providing for better vertical resolution of features in the lower levels. Unfortunately, the extra elevation angles that VCP 12 provides were not all available from the Kenai radar. The rapid scan feature of VCP 12 generated total volume scans about every 4 min, instead of the 6-min interval with VCP 21 and 10-min interval with VCPs 31 and 32 (Table VI). Table VI shows that VCP 31 was employed for the majority of the events following event 3. The decision to employ VCP 31 was based upon the assumption that it would be better suited to detecting ash particles due to its greater sensitivity, which is a result of the longer pulse length and slower revolution of the radar antenna [1].

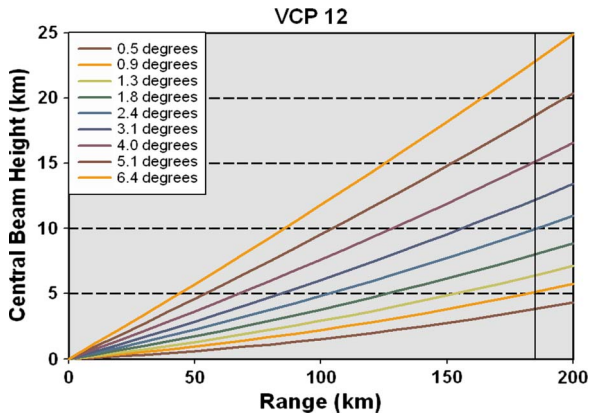

Fig. 5. Altitude of the Kenai radar beam as a function of the distance from the radar at various elevation angles relative to the VCP 12 volume coverage pattern (see Table V). The location of the Augustine Volcano is schematically indicated by a vertical line at 190 km from the radar. The beam height is measured in kilometers asl.

IV. RADAR OBSERVATIONS DURING AUGUSTINE ERUPTION

The following sections present the Augustine Volcano eruptive event 3, which occurred on January 13, 2006, from the perspective of the Kenai S-band weather radar data and show an application of the VARR-A retrieval algorithm to the data from the Kenai radar.

A. Radar Measurements of Augustine Eruption

As discussed earlier, the January 2006 eruption of Augustine Volcano consisted of a series of 13 explosive events. Each of these events was observed by the WSR-88D at Kenai. A single-polarized microwave weather radar is able to detect the measured average backscattered power P_{rH} at range r and is able to convert it into measured horizontally polarized radar reflectivity (factor) Z_{Hm} [mm^{6}m^{-3}] through [12]

$$Z_{Hm}(r) = C_R \frac{\overline{P}_{rH}(r)}{P_t L_H^2(r)} r^2 \tag{6}$$

where C_R is an instrumental constant, mainly dependent on the radar antenna and the receiver characteristics. For ash monitoring at microwave below 10 GHz, the path attenuation factor L_H due to particle and gas absorption along the ray is usually equal to about one.

A typical explosive event is event 3 (see Table VI), visualized using plane position indicator (PPI) radar images of the measured reflectivity in Figs. 6–8. The first two frames of Fig. 6 show the minutes preceding the explosion. Low reflectivity levels of around 5 to 15 dBZ are shown over the volcano, indicating that low levels of ash are being emitted. According to [25], the vulcanian explosion commenced at 13:24 universal time coordinate (UTC). This is indicated in the last frame at 13:28 UTC, when reflectivity levels above the volcano suddenly jump to 35 dBZ.

The peak of the event on radar occurs 4 min later (at 13:32 UTC), as in Fig. 7. Reflectivity values of 55 dBZ are occurring in the 0.5° range, and values of 35 dBZ occur in the 2.4° slice,

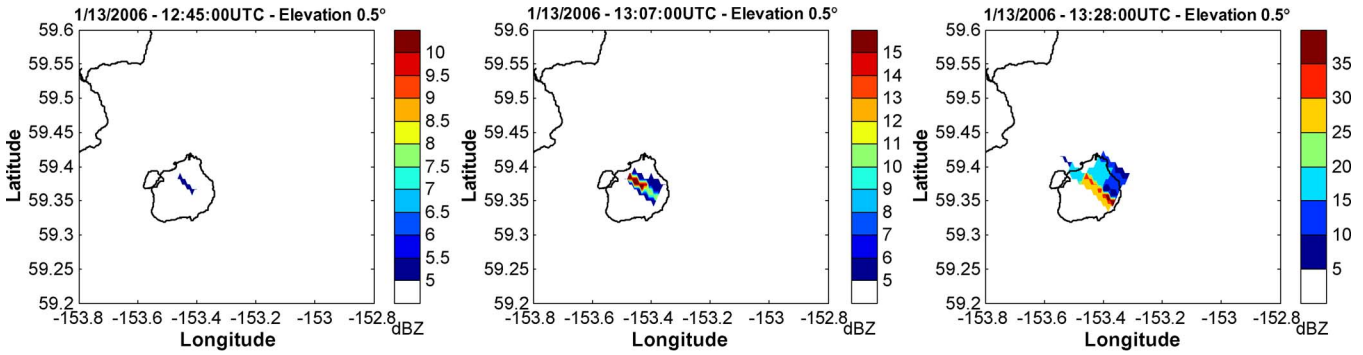

Fig. 6. PPI radar images at 0.5° elevation of the measured horizontally polarized reflectivity from 12:45 to 13:28 UTC—the onset of eruption event 3. The 35 dBZ maximum that occurs on the 13:28 UTC image takes place 4 min after the start of the explosive event.

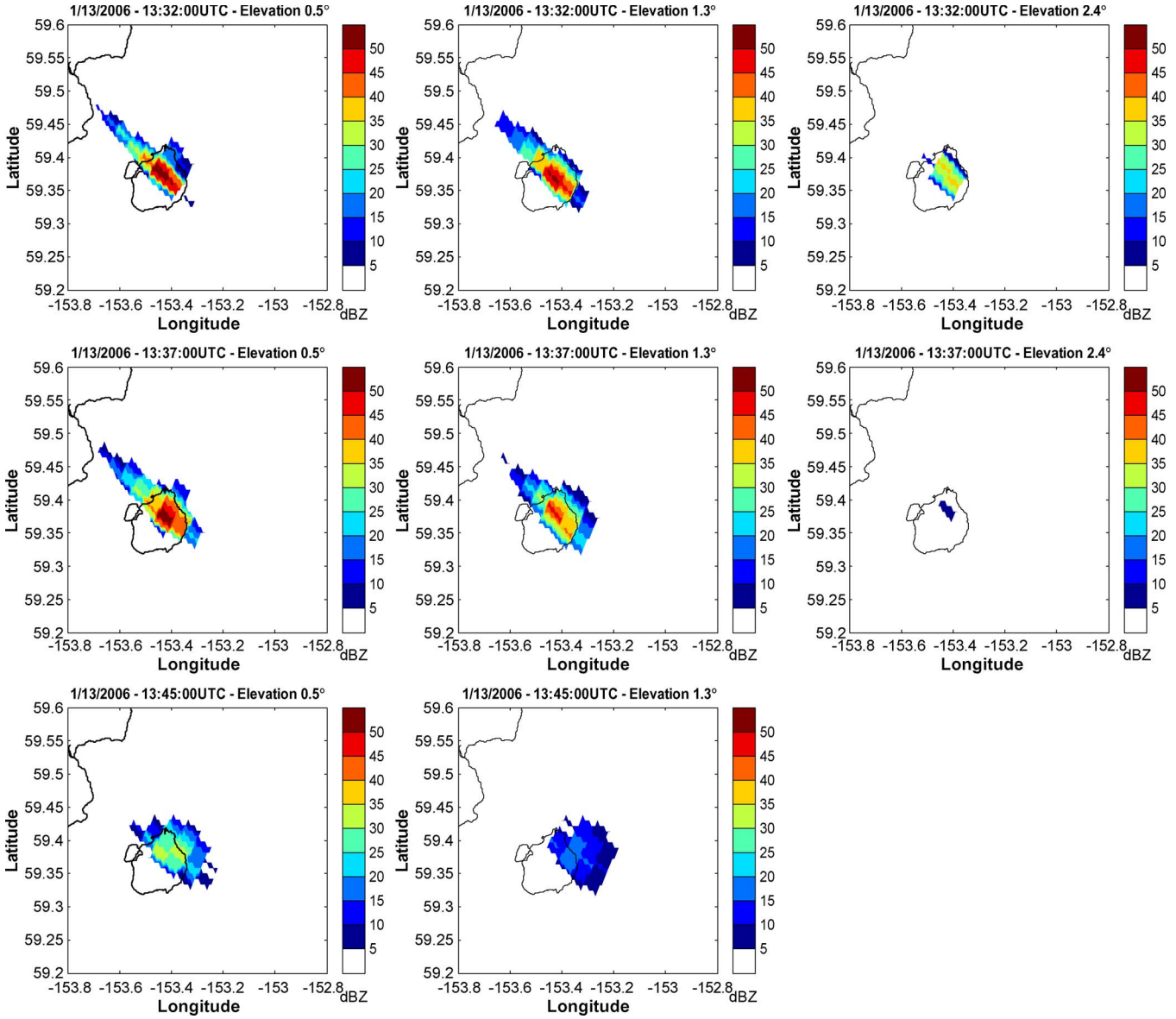

Fig. 7. PPI radar images for event 3 at (left column panels) 0.5°, (middle column panels) 1.3°, and (right column panels) 2.4° elevation of the measured horizontally polarized reflectivity from 13:32 to 13:45 UTC—the initial explosive phase of the eruption.

indicating that the volcanic plume has ascended to at least 10-km asl. The highest reflectivity values are limited to the lower portions of the plume (see Fig. 7). This may be due to the largest most reflective ash particles falling out of the plume at this level, while smaller particles continue to ascend to the 2.4° elevation slice. The 13:32 UTC frame represents the peak

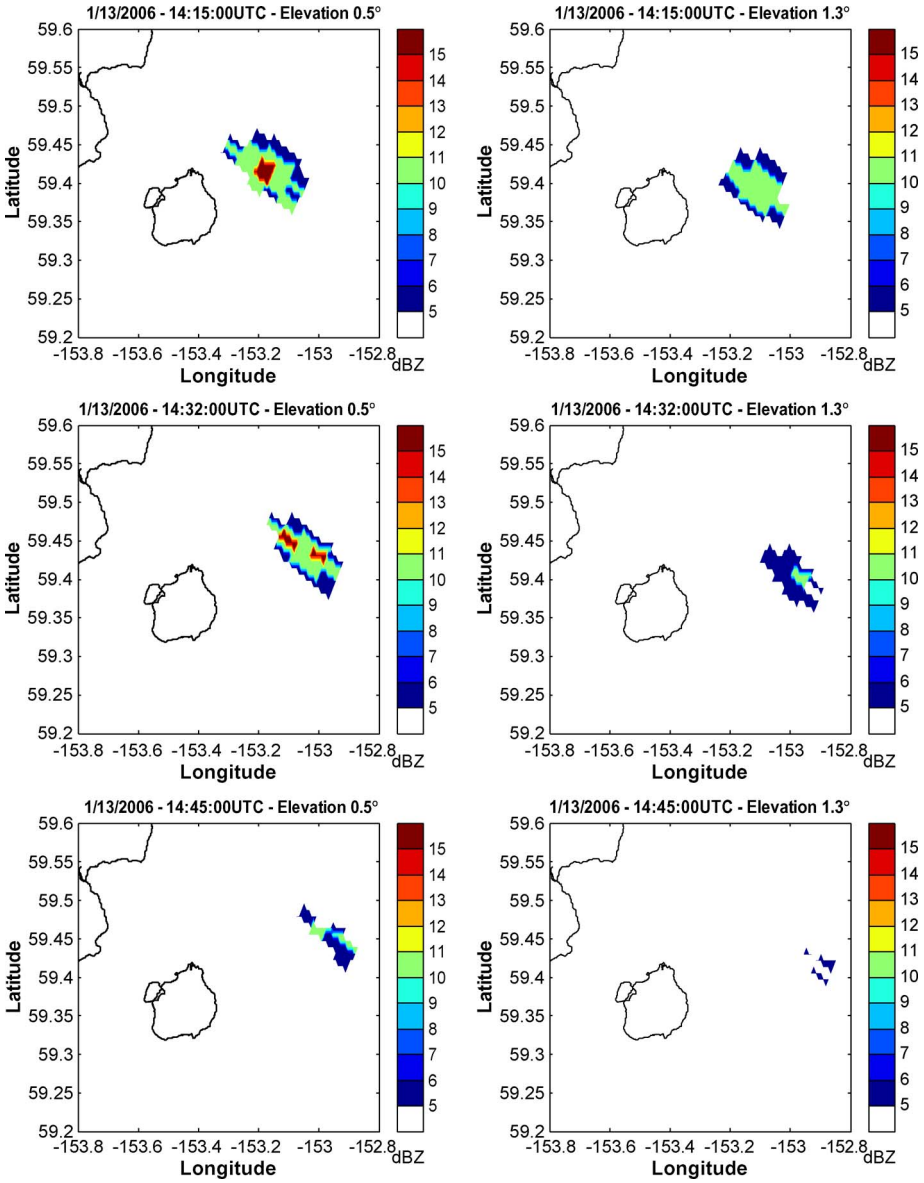

Fig. 8. PPI radar images for event 3 at (left column panels) 0.5° and (right column panels) 1.3° elevation of the measured horizontally polarized reflectivity from 13:58 to 14:54 UTC—the final phase of the eruption event.

of this event. By 13:37 UTC, the reflectivity in the 2.4° slice has diminished to around 5 dBZ, although reflectivities in the 0.5° slice remain intense, with values of around 50 dBZ. By 13:45 UTC, radar returns are absent from 2.4°, while maximum values have diminished further to 30 and 15 dBZ at the 0.5° and 1.3° slices, respectively. This drop in reflectivity indicates that the larger, heavier, and more reflective particles have fallen out of the ash plume.

The ice accretion on the ash particles, due to the abundant water vapor ejected with the ash, may justify the decrease in reflectivity observed because of the lower dielectric constant of ice, as discussed in [11]. The vertical profile of temperature derived from 12:00 UTC on January 13, 2006, radiosounding from Kodiak meteorological station, shown in Fig. 9, shows the altitude of the -15 °C isotherm to be around 2.4 km. Given that the lowest altitude reflectivity observed above Augustine is 3.9 km at 0.5° elevation, it can be inferred that all of the observed ash is subject to ice accretion processes.

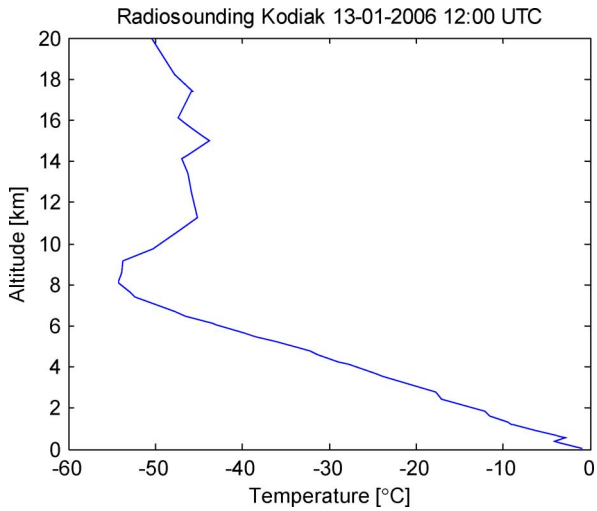

Fig. 9. Vertical profile of the temperature obtained by the local atmospheric radiosounding made at the Kodiak meteorological station on January 13, 2006, at 12:00 UTC.

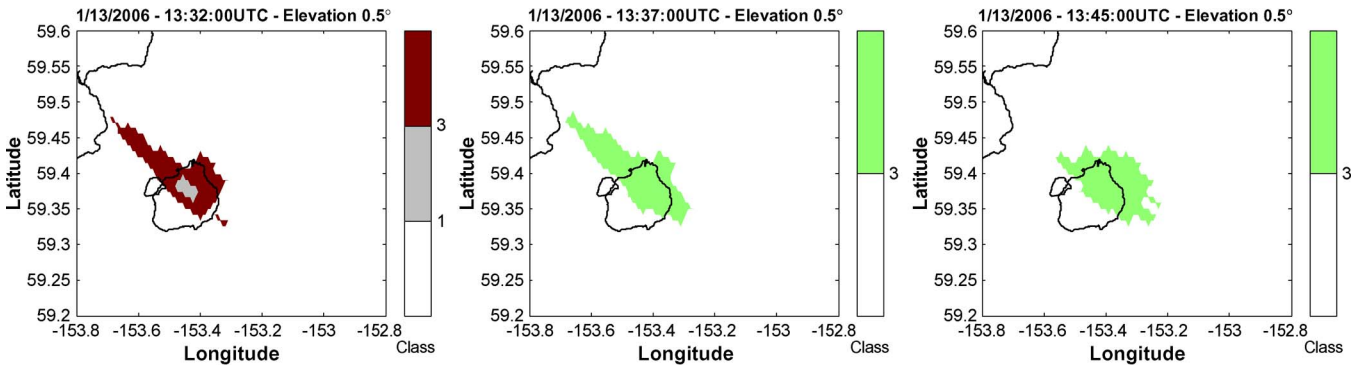

Fig. 10. PPI radar images for event 3 at 0.5° elevation of the estimated class index *Class*, which were derived from the PPI scan shown in Fig. 7 by applying the VARR-A classification algorithm—the initial explosive phase of the eruption. Class1 = large cold particle class. Class3 = small cold particle class.

After 13:45 UTC, the decline in reflectivity values and the height of the detected ash plume continues as the ash cloud moves away from the volcanic source, as shown in Fig. 8. Reflectivity values continue to diminish in both strength and altitude, as indicated by the more rapidly decreasing echoes in the higher elevation angles. Stronger reflectivities in the lower elevation angles, particularly 0.5°, may be due to the fallout from above. This is supported by the PPI radar images at 13:58 and 14:54 UTC, shown in Fig. 8. By 14:54 UTC, reflectivity returns are absent from the 1.3° elevation scan, and the measured reflectivity maximum value at 0.5° elevation is 5 dBZ. The diminishing of the reflectivity cores from the top down may suggest that the lower level returns are being sustained by fallout of heavier material from the upper levels of the ash plume.

It is important to recognize, however, that the disappearance of the ash plume from the radar does not signify the end of the ash threat. Infrared satellite imagery clearly showed the ash cloud from Augustine continuing northeast away from the volcano over 1 h after the cloud disappeared from the radar. By this point, the reduced concentration of ash, the gravitational removal of larger ash particles, and the ice nucleation and subsequent reduction of radar profile tend to render the cloud invisible to the WSR-88D [14]. In this respect, the synergetic role of satellite imagery in tracking volcanic ash, particularly after the initial stages of an eruptive event, becomes evident. Indeed, ground-based weather radar systems operating at a higher frequency, such as C- or X-band, or with a higher signal sensitivity might provide a better detection of ash clouds, even for low-concentration volcanic clouds [12].

B. Retrieval Results

The measured reflectivity images can be inverted to retrieve the ash aggregate concentration C_{px} by applying the radar retrieval technique VARR-A discussed in Section II. In the case of the Augustine eruption during the winter season, it may happen that ash nucleates ice early in ash cloud history; indeed, during the eruption, abundant water vapor was ejected, and the temperature was well below the freezing point also at the lower altitudes. We can expect that all observed ash is subject to ice accretion processes, and we must assume within the radar microphysical forward model that ash clouds are made by solid ash, hydrometeors, and ash aggregates, which are made by a mixture of ash and ice. The temperature for each radar bin is evaluated by means of the vertical radiosounding profile shown in Fig. 9, taken in the proximity of the Augustine Volcano from the Kodiak meteorological station. We will assume this vertical temperature profile as reference data for the classification technique.

No cloud and precipitation patterns were present prior to the Augustine eruption on January 13, 2006 [1]. Geostationary mid-infrared imagery showed a winter that is relatively humid. If the classification algorithm given in (3) is applied, for example, to the radar PPI data for event 3 at 0.5° elevation, shown in Fig. 7, we can detect the class associated with every range bin and shown in Fig. 10. We note that, from 13:32 to 13:45 UTC, the reflectivity is predominantly associated with the small cold class (class = 3), which corresponds, from Fig. 1, to an average reflectivity of about 37 dBZ (whereas the average reflectivity of the large cold class is about 76 dBZ). The same result is obtained at all times and at all elevation angles. It means that every range bin of the volume scan radar data has been included from the classification algorithm into the cold category. Indeed, this is expected because of the environmental conditions of the considered area.

As a further step, Fig. 11 shows the results in terms of estimated particle mass concentration C_{px}, which is obtained by applying the estimation technique given in (4) to the measured reflectivity PPI data. The maximum value of C_{px} is 0.5 kg m^{-3}, which is assumed in the PPI representation of the estimated mass concentration at 0.5° elevation, in correspondence of the reflectivity peak of 55 dBZ occurring in the 0.5° range at 13:32 UTC (see Fig. 7).

It is evident that the C_{px} estimated patterns resemble the measured Z_H PPI pattern [12]. Since the class associated with each range bin corresponds to the small cold particle category, high/low reflectivity values are always associated with large/small concentration of particles within the volcanic cloud, as expected from Fig. 1. The same considerations can be made at all other times and elevation angles. Due to the inversion developed in Section II, we are not able to identify the ash fraction within the aggregate concentration as the single-polarization radar reflectivity is not sensitive to the particle composition [11].

Starting from the results from the retrieval algorithm of the estimated mass particle concentration within the volcanic cloud at all times and at all elevations and using the information about the scanning strategy employed during the eruptive

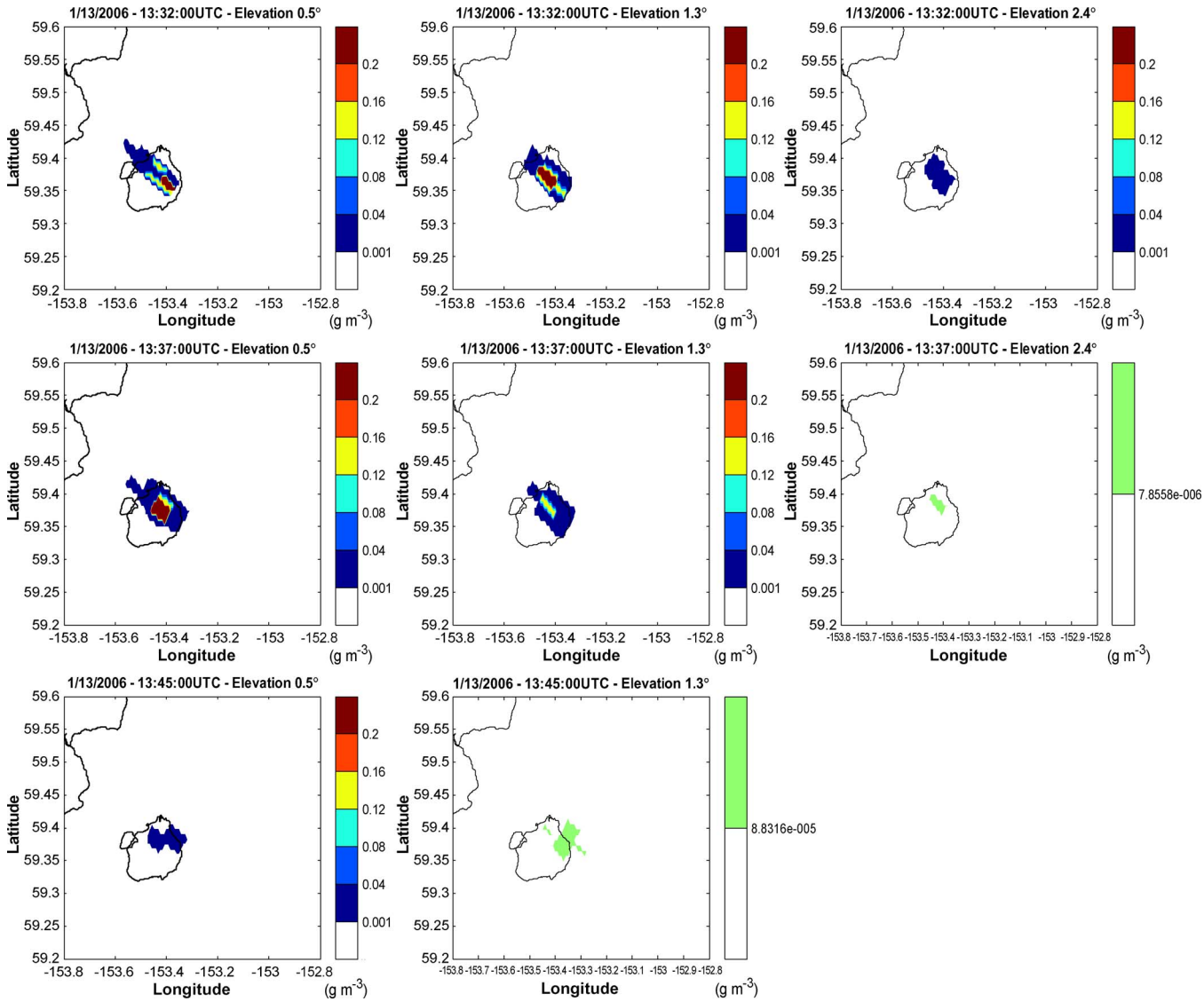

Fig. 11. PPI radar images of the estimated ash aggregate concentration for event 3 at (left column panels) 0.5°, (middle column panels) 1.3°, and (right column panels) 2.4° elevation from 13:32 to 13:45 UTC—the initial explosive phase of the eruption.

event 3 observation, we have also estimated the radar retrieved columnar content of eruptive material. Fig. 12 shows the PPI-referred mass content of the eruptive material retrieved by the Kenai radar at 0.5°, 1.3°, and 2.4° elevations and the total retrieved mass content considering all PPIs, with respect to time, during the observation of explosive event 3. The peak of the total retrieved columnar content at 13:32 UTC corresponds to the vulcanian explosive phase when a larger amount of eruptive material is ejected. In this phase, the estimated particle concentration within the ash cloud and, consequently, the total mass content assume their maximum values. Note that the scan geometry of the Kenai radar (see Fig. 5) limits mass integration to heights higher than 4 km at a range of 190 km around the Augustine Volcano.

V. Conclusion

The potential of using ground-based weather radar systems for volcanic ash cloud detection and quantitative retrieval has been evaluated. The volcanic cloud radar remote sensing has been based on a physically based retrieval scheme, named VARR-A. The training simulations of the volcanic cloud radar reflectivity have been performed using Z-ATHAM, which is a Mie backscattering scheme coupled with the ATHAM plume numerical model. The relationship between radar reflectivity factor and ash aggregate concentration has been derived for the various particle classes, including aggregates of ice and water hydrometeors with ash. The volcanic cloud retrieval physical-statistical algorithm has been designed, exploiting a Bayesian classification and an optimal regression technique.

An application of the VARR-A retrieval technique has been shown, using as case study the Augustine Volcano eruption in January 2006. This event was a significant sub-Plinian volcanic eruption observed within the nominal range of the NEXRAD WSR-88D S-band radar, located in Kenai, which is 190 km from the volcano vent. This eruption provided a unique opportunity to showcase the capabilities of the WSR-88D in a context other than that for which the radar was originally designed.

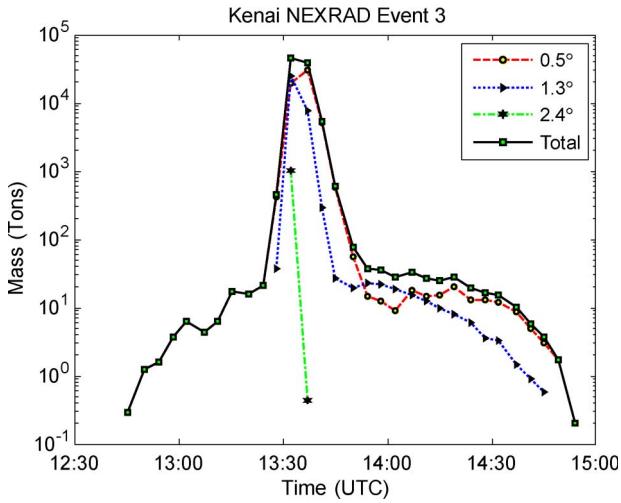

Fig. 12. PPI-referred mass content of the eruptive material retrieved by the Kenai radar at 0.5°, 1.3°, and 2.4° elevations and the total retrieved mass content (from all PPIs) with respect to time during the observation of explosive event 3. The total retrieved columnar content is given from the sum of the columnar contents estimated for the elevation scans at the three elevation angles that are provided from VCP 12 and that are available from the Kenai radar.

The radar data, in conjunction with pilot reports, proved to be crucial in analyzing the height and movement of volcanic ash clouds during and immediately following each eruptive event.

Data from the Kenai weather radar have been processed to identify and estimate particle concentration. Starting from the reflectivity PPI data, the classification step identified the class associated with every range bin, while in the second step, the mass concentration has been estimated into the ash cloud. Using the scanning strategy employed during the eruptive event observation, the radar retrieved mass content of eruptive material has also been estimated. Currently, there is no capability to extrapolate the ash portion within the identified aggregate using conventional radars. The case study has been analyzed in terms of its evolution by looking at both radar measurements and ash products derived from the measurements themselves. The analysis has clearly shown the unique feature of radar remote sensing of volcanic eruptions, especially for remote sites where the ground collection of ash is almost impossible as for the Augustine Volcano (surrounded by the sea; see Fig. 3).

Future developments will be devoted to the exploitation of the retrieval scheme VARR-A for operational weather radar that is close to other active volcanoes. The algorithms employed in this paper have been developed using results of Z-ATHAM simulations. A future work should also consist of testing these retrieval algorithms on data from *in situ* measurements. The Z-ATHAM model might be generalized to include a variability in terms of temperature environment and eruption processes (e.g., magmatic or phreato-magmatic cases). The VARR-A approach might refer to a preset "library" of Z-ATHAM simulations that are specific for each site and season of interest. An automatic classification of the eruptive scenario might help in solving some difficulties due to ambiguities in detecting aggregation processes. Complementary information coming from local and satellite sensors is essential to this purpose, and the Bayesian framework can easily incorporate it.

By using single-polarization weather radar, it is fairly difficult to discriminate between ash, hydrometeors, and mixed particles. To do this, we should use a dual-polarized weather radar that is capable of measuring polarimetric observables. If these polarimetric data were available, strong improvements of the obtained retrievals could be achieved by taking into account not only the particle mixed composition but also their shape. In this respect, weather radar at X-band might show even a better sensitivity with respect to corresponding S- and C-band systems having the same characteristics. Finally, a portable weather radar system might overcome the limitation of observing a volcanic eruption from far distances as in the case study considered here.

APPENDIX A
ATHAM NUMERICAL PLUME MODEL

The ATHAM model explicitly simulates the dynamics (including turbulence) and thermodynamics within the eruption column and in the ambient atmosphere during eruption and shortly afterward [27]–[30]. In contrast to typical atmospheric models where particles are passively transported, in ATHAM, the effect of ash and hydrometeors on the dynamics is considered. In the configuration used in this paper, ATHAM is set up in cylindrical coordinates within an azimuthally symmetric domain in order to save computer resources. Simulations in cylindrical coordinates reproduce, indeed, the results from 3-D simulations without crosswind [27].

ATHAM Microphysical Processes: In addition to cloud microphysics for liquid and frozen hydrometeors, ATHAM considers the microphysics of volcanic ash and the aggregation of volcanic particles. The scheme is a modal approach, and two moments of the size distribution, namely, *mass mixing ratio* and *number concentration*, are explicitly calculated as prognostic variables [31], [32]. The microphysical formulation is based on the microphysical concept for usual atmospheric (meteorological) clouds, with the extension that volcanic particles can be contained in all categories of hydrometeors forming mixed hydrometeor-ash particles. The ATHAM model does not consider the coexistence of dry ash, pure hydrometeors, and mixed aggregates at the same location at a given model time step. Particles are all treated like rigid equivalent spheres because the information about their shapes is limited and the spherical model simplifies the microphysical treatment.

The shape effect on the fall velocity is only considered by applying a drag coefficient. Coalescence of hydrometeor-ash aggregates is assumed to be a function of the hydrometeor mass fraction within the mixed particles. Apart from water vapor, we can consider the mass mixing ratios q of four categories hx of hydrometeors and four categories ax of ash as prognostic variables ($x = 1$-4). The composition of these aggregates is a total mixing ratio q_{px} (in kilogram per kilogram), given by the sum of the mass mixing ratios of ash q_{ax} and hydrometeors q_{hx}

$$q_{px} = q_{hx} + q_{ax}. \tag{A1}$$

TABLE VII
PARTICLE CATEGORIES CONSIDERED IN THE ATHAM MODEL

x	Class label	Hydrometeor	Ash	Aggregate
1	Small warm	Cloud water	Small ash at $T>T_0$	Ash/Water
2	Small cold	Cloud ice	Small ash at $T<T_0$	Ash/Ice
3	Large warm	Rain	Large ash at $T>T_0$	Ash/Water
4	Large cold	Graupel	Large ash at $T<T_0$	Ash/Ice

The first column is class index. The second column refers to pure hydrometeors, the third to pure ash, and the right to mixed hydrometeor–ash particles. T_0 is the freezing temperature.

Note that these particles with subscript px can be either dry ash or pure hydrometeors or mixed hydrometeor-ash particles (aggregates), depending on the relative concentration of ash and hydrometeor given in (A1).

Table VII gives an overview of the particle categories. In ATHAM, the volcanic ash, erupted at the vent, is initialized in the two warm categories. The size distribution is represented by the superposition of the two modes. As soon as the temperature T in the rising eruption column falls below its freezing level value T_0, pure volcanic ash is reclassified to the corresponding cold categories (see Table VII). If the ash is contained in mixed hydrometeor-ash aggregates, it undergoes the same microphysical processes as hydrometeors. That means, for example, that freezing of water to ice in a mixed particle also transfers the warm ash to the respective cold ash category. The density ρ_{px} (in kilograms per cubic meter) of mixed hydrometeor-ash particles is obtained from the volume ratio of ash and water as a mixing-ratio weighted formula

$$\rho_{px} = \rho_{ax}\rho_{hx}\frac{q_{hx}+q_{ax}}{\rho_{ax}q_{hx}+q_{ax}\rho_{hx}}. \tag{A2}$$

Water and ash are assumed to have a density of 1000 and 1800 kg/m^3, respectively, whereas ice and graupel have individual densities of 917 and 500 kg/m^3 [34]. Like all other qualities of mixed particles, the density also converges to that of the pure material in the absence of the other.

Microphysical Characterization: In our modal microphysical parameterization, the PSD of each mode is assumed to follow a generalized gamma function [14], [19]. We can assume the following: 1) the particles are spherical or equivalent spherical with a constant density ρ_{px}, and 2) the minimum and maximum particle radii are zero and infinite. The modified-gamma PSD $N_{px}(r)[\mathrm{m}^{-3}\mathrm{mm}^{-1}]$ for a generic class of particles px with radius r, which describes particle occurrence per unit volume and unit size, is expressed by multiplying the normalized function $F_G(r)$ [1/mm] by the number concentration N_{npx} [1/kg] and the specific density of particles ρ_{px} (in kilograms per cubic meter)

$$\begin{aligned} N_{px}(r) &= \rho_{px}N_{npx}F_G(r) \\ &= \frac{\rho_{px}N_{npx}}{\Gamma(\nu_{px})r_{npx}}\left(\frac{r}{r_{npx}}\right)^{\nu_{px}-1}e^{-\frac{r}{r_{npx}}}. \end{aligned} \tag{A3}$$

In (A3), $F_G(r)$ is the probability to find a particle of a certain radius r [in millimeter], and υ_{px} is the dimensionless skewness parameter of the size distribution. The expression $\Gamma(\upsilon_{px})$ is the complete gamma function of υ_{px}, and it arises from the normalization of $F_G(r)$ to one. The *characteristic radius* r_{npx} is dependent on the mass mixing ratio q_{px} and the total number concentration N_{npx} of the particles px with the specific density ρ_{px}

$$\frac{4}{3}\pi(r_{npx})^3\rho_{px} = \frac{q_{px}\rho_{px}}{N_{npx}}\frac{\Gamma(\nu_{px})}{\Gamma(\nu_{px}+3)}. \tag{A4}$$

From (A4), r_{npx} may also be interpreted as an *equivalent* particle radius giving the same PSD total mass.

The values of υ_{px}, $\Gamma(\upsilon_{px})$, and $r_{n,px}$ are constant at a given grid point during one model time step of the numerical experiment. To solve the equations for the particle aggregation processes, the complete moment m_{Fk} of order k of $F_G(r)$ is useful and is expressed as

$$m_{Fk} = \int_0^\infty r^P F_G(r)dr = r_{npx}^k\frac{\Gamma(\nu_{px}+k)}{\Gamma(\nu_{px})}. \tag{A5}$$

The *mass concentration* C_{px} (in grams per cubic meter) of each particle is given by

$$C_{px} = 10^{-6}\int_0^\infty \frac{4}{3}\pi\rho_{px}r^3N_{px}(r)dr = 10^3C_pq_{px} \tag{A6}$$

and the *total mass concentration* C_p is defined as

$$C_p = \sum_{x=1}^{4} C_{px} \tag{A7}$$

where the class index x goes from one to four (see Table VII).

The selection of the skewness parameters ν_{px} in (3) is rather difficult since a very few observations of size distributions are available, especially for particles in volcanic eruption columns. We assume $\upsilon_3 = 3.5$, as observed by [35] for rain $(x = 3)$ in usual meteorological clouds. Because of the lack of information about ice particle qualities and for simplicity, the same skewness parameter $\upsilon_4 = 3.5$ is applied for graupel $(x = 4)$. The size distributions of cloud water and cloud ice ($x = 1$ and $x = 2$, respectively) are described with $\upsilon_1 = \upsilon_2 = 16$, as used by [19] and [36] for typical continental clouds with high concentrations of condensation nuclei. For the ash, the analysis of available measured PSDs taken from data sets in [33] led to the result that the most probable value of the skewness parameter is $\upsilon_{ax} = 1$ for all classes $x = 1$-4. The skewness parameters of the size distributions of mixed hydrometeor-ash particles υ_{px} should be dependent on the formation process and on relative mass fractions of hydrometeors and ash. Because no observational data exist, it is obtained from linear interpolation with respect to the mass fraction of ash and water in this paper

$$\nu_{px} = \frac{q_{ax}\nu_{ax}+q_x\nu_{hx}}{q_{ax}+q_{hx}} \tag{A8}$$

where the terms in (A8) have already been defined.

APPENDIX B
RADAR RESPONSE SIMULATION FROM ATHAM

The numerical experiments performed with ATHAM begin just after the earliest mixing of the erupting gas–particle

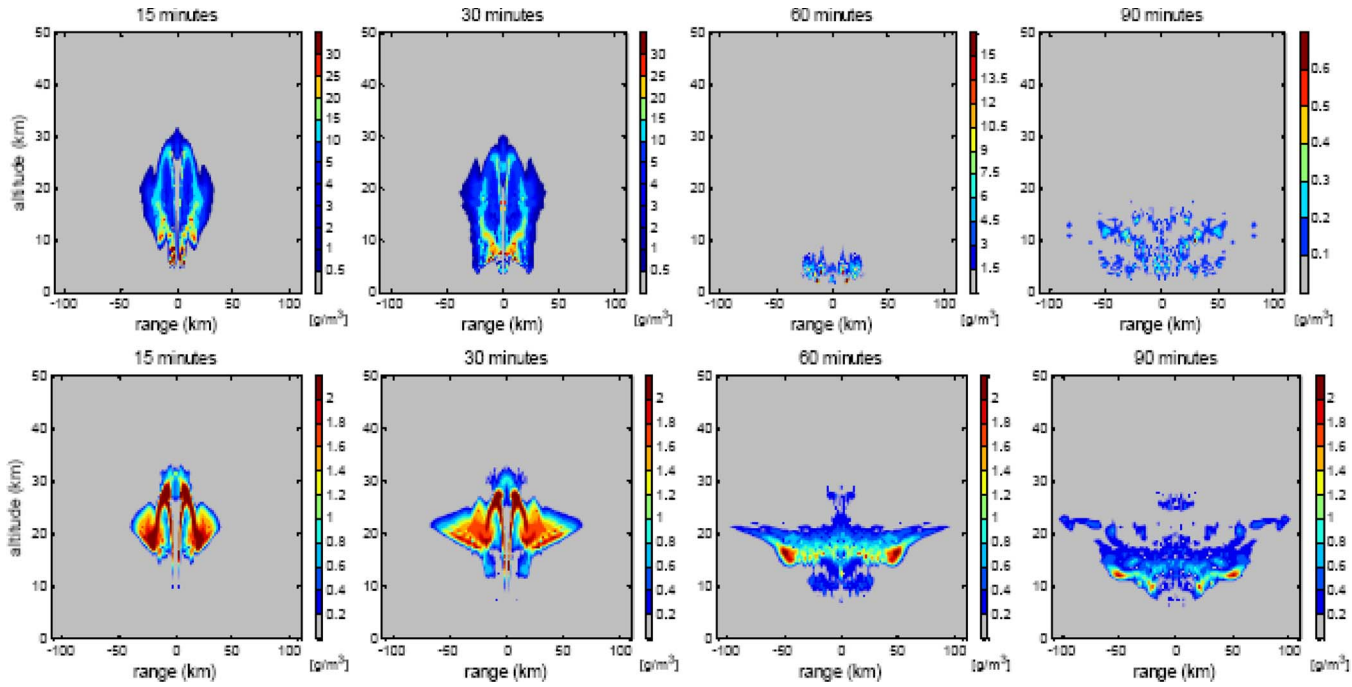

Fig. 13. Mass concentration C_{px} ($x-z$ distributions) of particles (hydrometeors, ash, and aggregates) in the (top row panels) large and (bottom row panels) small cold particle modes, shown at 15, 30, 60, and 90 min for the sensitivity experiment EXP3. The uniform color-bar scale gives mass concentration in grams per cubic meter. Specular symmetry is due to the ATHAM simulation setup (see text for details).

mixture with ambient air, when the flow adjustment to atmospheric pressure has already taken place. We do not try to simulate a specific eruption but choose conditions typical for highly explosive events. The results from our experiments are suitable in investigating the principal features of a volcanic eruption column. The experiments are performed on a stretched grid with 150 $\times$ 80 points. The model domain is 300 km in the horizontal and 50 km in the vertical direction.

ATHAM Simulation Results: The microphysics of hydrometeors and ash particles in a Plinian volcanic eruption column has been studied by performing some numerical experiments with the ATHAM model [20]. These numerical experiments adopt a PSD similar to that observed during the eruption of Mt. St. Helens (1980) [27]. In these ATHAM simulations, the eruption lasts 30 min, whereas the model runs for another 60 min to simulate the posteruptive phase. Due to ATHAM azimuthal symmetry, cloud sections are always specular with respect to the vertical axis passing through the origin. One cross section through $y = 0$ is calculated, i.e., through the center of the model domain, where the volcano is situated.

We have performed three similar numerical experiments under the same conditions except for the initial particle size r_{in}. The tags of the ATHAM numerical experiments and the initial characteristic radius r_{inS} and r_{inL} of ash average mass, respectively, in the small and large classes for each experiment are the following:

1) EXP1 (small mode r_{inS}: 10 μm; large mode r_{inL}: 100 μm);
2) EXP2 (small mode r_{inS}: 50 μm; large mode r_{inL}: 250 μm);
3) EXP3 (small mode r_{inS}: 100 μm; large mode r_{inL}: 500 μm).

In the simulated Plinian eruption columns, ice was highly dominant in comparison to liquid water ($>$ 99% by mass). This was caused by the fast column rise ($>$ 100 m/s on average) to regions well above the freezing level (at 5-km altitude in ATHAM simulations). The particles occur mainly as fairly dry icy ash aggregates. The aggregation of wet or icy ash due to gravitational capture resulted in efficient aggregation and increased the particle fall velocities.

Fig. 13 shows the results of EXP3, which is the most representative experiment, in terms of particle mass concentration C_{px} for the two cold particle dimension modes at different times during the simulation. Two distinct regions of ash develop in our experiments, as shown in Fig. 13, caused by the separation of the fine fraction (and gases) suspended in a thin layer at an HNB of around 20 km from a deep settling layer of coarser particles in the larger class. In EXP3, the increased particle size in the larger class and the greater differences of the sizes and fall velocities between the two classes cause a significantly enhanced particle growth because gravitational capture becomes more efficient. Consequently, accretion process and sedimentation are generally much more pronounced in EXP3 than in the EXP1 experiment. We can conclude that an extended knowledge on the initial PSD is crucially needed in order to assess the ash dispersal during explosive volcanic eruptions.

1) Radar Reflectivity Simulations: Rayleigh scattering approximation is applicable for small size parameters ξ (i.e., $\xi = kr \ll 1$, with r as the particle radius and k as the wavenumber). If a Rayleigh scattering regime holds, from (A3), the radar reflectivity factor Z_{px} due to an ensemble

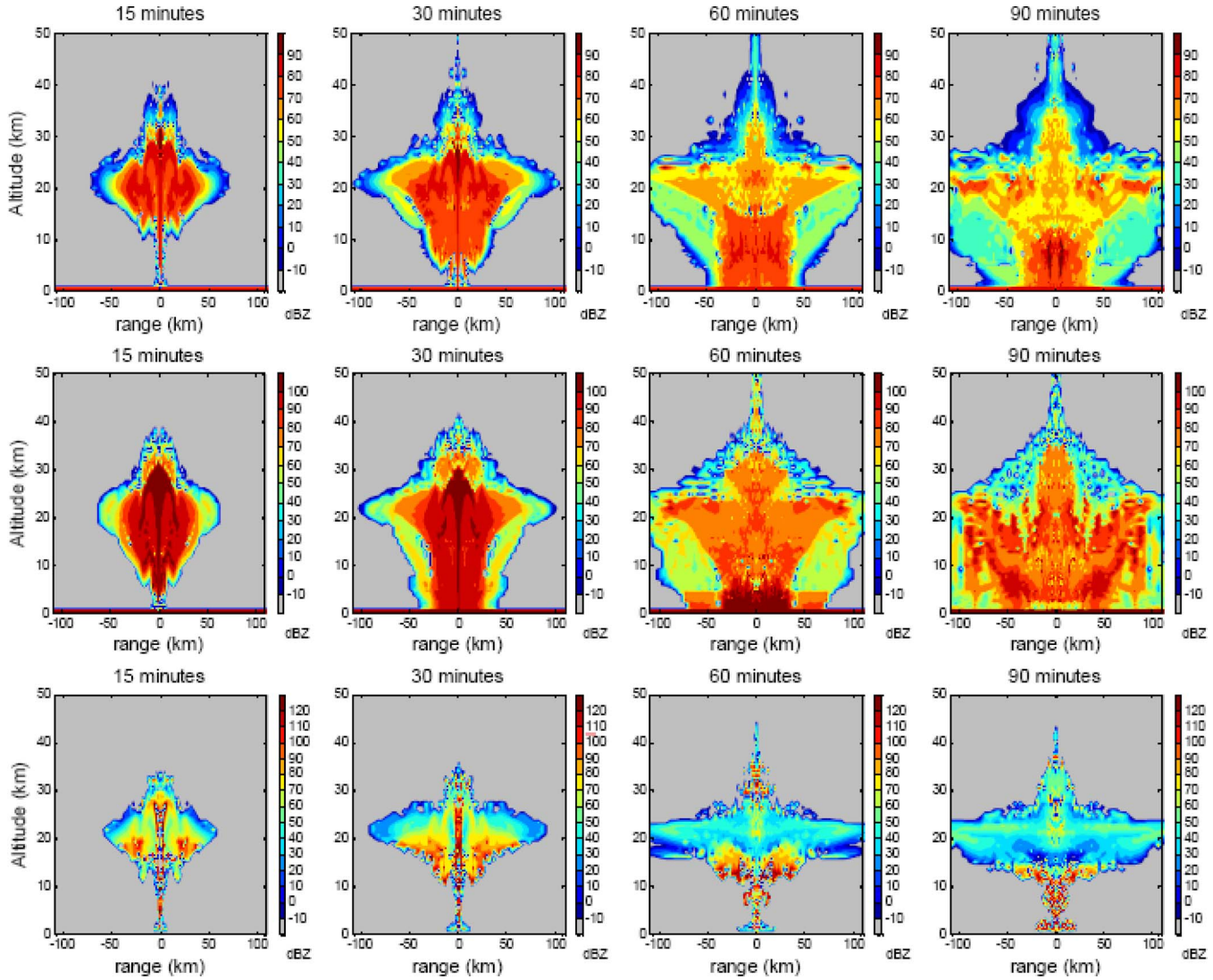

Fig. 14. Total reflectivity factor Z_p ($x-z$ distributions) of the eruption cloud particles (hydrometeors, ash, and aggregates) shown after 15, 30, 60, and 90 min, for (top row) numerical experiment EXP1, (middle row) EXP3, and (bottom row) NOAGG. Note the slightly different scale (in dBZ) for the three numerical experiments.

of particles px is expressed as the sixth moment of PSD as follows [36]:

$$Z_{px} = \eta_{px} \frac{\lambda^4}{\pi^5 |K_{px}|^2} = \int_0^\infty D^6 N_{px}(D) dD \qquad \text{(B1)}$$

with $D = 2r$ as the particle diameter. In (B1), η_{Hpx} (in per meter) is the radar volumetric reflectivity, λ is the radar wavelength, and K_{px} is the dielectric factor of the particle ensemble of category x, depending on the particle dielectric constant ε_{px} [14]. Using (A3), the previous equation reduces to the following analytical expression:

$$Z_{px} = 64 \rho_{px} N_{npx} r_{npx}^6 \frac{\Gamma(\nu_{px} + 6)}{\Gamma(\nu_{px})}. \qquad \text{(B2)}$$

The total reflectivity factor Z_p is the sum of the backscattered power due to the various aggregates

$$Z_p = \sum_{x=1}^{4} Z_{px}. \qquad \text{(B3)}$$

Note that the radar reflectivity factor Z_p, expressed in mm^6m^{-3}, is sometimes expressed in logarithmic power (dBZ) and often simply referred to as radar reflectivity.

The set of the numerical experiments, analyzed in the previous section, permits us to investigate the sensitivity of the radar response to particle aggregation processes within the eruptive column. The results of the Z-ATHAM simulations EXP1, EXP3, and No Aggregation (NOAGG), in terms of total reflectivity Z_p, are shown in Fig. 14. We must consider that, in the NOAGG experiment, having switched off ash aggregation, the reflectivity factor is calculated, summing at each grid point contributions due to hydrometeors and ash, so that the expression for each of the four particle classes is $Z_{px} = Z_{hx} + Z_{ax}$. Particle reflectivity values in the EXP3 experiment are higher, on average, than those in EXP1 and NOAGG. This is quantitatively confirmed by inspecting Fig. 14, where the occurrence of higher reflectivity values in EXP3 is evident at all simulation times. This is due to the fact that the reflectivity increases with increasing particle size. The particle aggregation process is much more relevant in EXP3 than in the EXP1

experiment. Moreover, in EXP3, the sedimentation is much more pronounced, and falling of larger and more reflective particles at the end of the simulation generates higher reflectivity values at the eruption column base, where the settling coarser particles are more concentrated. Sedimentation is least significant in NOAGG, where particles remain small.

A basic question arises whether the Rayleigh model, summarized in (B1), may be adopted for ash retrieval at all microwave bands. In a previous work, we showed that, for solid ash, the Rayleigh scattering approximation is adequate for sizes of up to few millimeters at X-band [14]. In the presence of hydrometeor and ash aggregates, this conclusion may be less appropriate, and the general Mie scattering solution should be claimed [37]–[39]. The Mie theory for spherical particles requires the complex refractive index $n = \sqrt{\varepsilon_{rx}}$ as input parameter, where ε_{rpx} is the complex relative dielectric constant (or permittivity) of the particle material. For liquid water permittivity ε_{rhx}, we have used the Liebe model [40], whereas the relative dielectric constant of solid ash that is equal to $\varepsilon_{rax} = 6\text{-j}0.175$ is assumed for all frequency bands and all particle classes [41]. Even though various mixture models are available (e.g., see [14]), similar to (A7), the permittivity of mixed hydrometeor-ash particles ε_{rpx} is obtained here from a linear interpolation with respect to the mass fraction of ash and water

$$\varepsilon_{rpx} = \frac{q_{ax}\varepsilon_{rax} + q_{hx}\varepsilon_{rhx}}{q_{ax} + q_{hx}}. \tag{B4}$$

Similar to the Rayleigh scattering theory and neglecting polarization, it is possible to introduce an *equivalent* reflectivity factor Z_{epx} for each particle class, computing the Mie backscattering cross section σ_b. Under the Mie's scattering regime, the radar reflectivity factor is a function of frequency, particle dielectric constant, and PSD.

Numerical simulations have been used to evaluate the difference $\Delta Z_{px} = Z_{px} - Z_{epx}$ between the reflectivity factor Z_{px} computed using Rayleigh scattering approximation as in (B1) and the Z_{epx} derived from the Mie theory for the four particle classes and the EXP3 simulation. The statistical indexes of this difference are the mean value $MV = \langle \Delta Z_{px} \rangle$ and the root mean square $RMS = \sqrt{\langle \Delta Z_{px}^2 \rangle}$. In EXP1, where the particle sizes are smaller, the Rayleigh scattering condition is always well satisfied up to the X-band radar observations for all classes, being the mean value of the difference ΔZ_{px}, for the large classes, which is smaller than 0.1 dBZ up to the X-band. In EXP3, at S-band, the mean value of ΔZ_{px} is always less than 0.6 dBZ. Contrarily, at C- and X-band, there is a stronger difference of radar reflectivity responses for large class observations, which means that the Rayleigh condition is no longer valid at these bands and that Mie effects are no longer negligible.

ACKNOWLEDGMENT

The authors would like to thank H. G. Graf and M. Herzog (University of Cambridge, U.K.) for their helpful suggestions, B. De Bernardinis (DPC, Italy) for the continuous support, S. Barbieri (Sapienza University of Rome, Rome, Italy) for the computational help, the Alaska NEXRAD team and the U.S. Geological Survey staff of the Alaska Volcano Observatory (AK) for providing the NEXRAD WRD-88D radar data of the Augustine Volcano eruption in a readable format, and the two anonymous reviewers for their useful suggestions.

REFERENCES

[1] G. L. Hufford, L. J. Salinas, J. J. Simpson, E. G. Barske, and D. C. Pieri, "Operational implications of airborne volcanic ash," *Bull. Amer. Meteorol. Soc.*, vol. 81, no. 4, pp. 745–755, Apr. 2000.

[2] T. J. Grindle and F. W. Burcham, Jr., "Engine damage to a NASA DC-8-72 airplane from a high-altitude encounter with a diffuse volcanic ash cloud," NASA, Washington, DC, NASA Tech. Memo TM-2003-212030, 2003.

[3] J. Wood, C. Scott, and D. Schneider, "WSR-88D radar observations of volcanic ash, World Meteorological Organization," in *Proc. 4th Int. Workshop Ash*, Rotorua, New Zealand, Mar. 26–30, 2007.

[4] C. J. Horwell and P. J. Baxter, "The respiratory health hazards of volcanic ash: A review for volcanic risk mitigation," *Bull. Volcanol.*, vol. 69, no. 1, pp. 1–24, Jul. 2006.

[5] M. V. Stasiuk, C. J. Hickson, and T. Mulder, "The vulnerability of Canada to volcanic hazards," *Nat. Hazards*, vol. 28, no. 2/3, pp. 563–589, Mar. 2003.

[6] F. S. Marzano, E. Picciotti, G. Ferrauto, G. Vulpiani, and W. I. Rose, "Volcanic ash remote sensing by ground-based microwave weather radar," in *Proc. Gen. Assem. Eur. Geosci. Union*, Vienna, Austria, Apr. 2005.

[7] J. J. Simpson, G. Hufford, D. Pieri, and J. Berg, "Failures in detecting volcanic ash from a satellite-based technique," *Remote Sens. Environ.*, vol. 72, no. 2, pp. 191–217, May 2000.

[8] W. I. Rose, G. J. S. Bluth, and G. G. J. Ernst, "Integrating retrievals of volcanic cloud characteristics from satellite remote sensors: A summary," *Philos. Trans. R. Soc. London A, Math. Phys. Sci.*, vol. 358, no. 1770, pp. 1585–1606, May 2000.

[9] T. Yu, W. I. Rose, and A. J. Prata, "Atmospheric correction for satellite based volcanic ash mapping and retrievals using split-window IR data from GOES and AVHRR," *J. Geophys. Res.*, vol. 107, no. D16, p. 4311, Aug. 2002.

[10] F. Prata, G. Bluth, B. Rose, D. Schneider, and A. Tupper, "Comments on 'Failures in detecting volcanic ash from a satellite-based technique'," *Remote Sens. Environ.*, vol. 78, no. 3, pp. 341–346, Dec. 2001.

[11] C. Lacasse, S. Karlsdóttir, G. Larsen, H. Soosalu, W. I. Rose, and G. G. J. Ernst, "Weather radar observations of the Hekla 2000 eruption cloud, Iceland," *Bull. Volcanol.*, vol. 66, no. 5, pp. 457–473, Jul. 2004.

[12] F. S. Marzano, S. Barbieri, G. Vulpiani, and W. I. Rose, "Volcanic cloud retrieval by ground-based microwave weather radar," *IEEE Trans. Geosci. Remote Sens.*, vol. 44, no. 11, pp. 3235–3246, Nov. 2006.

[13] F. S. Marzano, E. Picciotti, G. Ferrauto, G. Vulpiani, and W. I. Rose, "Volcanic ash remote sensing by ground-based microwave weather radar," in *Proc. Gen. Assem. EGU*, Vienna, Austria, Apr. 25–29, 2005, pp. 212–215.

[14] F. S. Marzano, G. Vulpiani, and W. I. Rose, "Microphysical characterization of microwave radar reflectivity due to volcanic ash clouds," *IEEE Trans. Geosci. Remote Sens.*, vol. 44, no. 2, pp. 313–327, Feb. 2006.

[15] W. I. Rose, D. Delene, D. Schneider, G. Bluth, A. Krueger, I. Sprod, C. McKee, H. Davies, and G. Ernst, "Ice in the 1994 Rabaul eruption cloud: Implications for volcano hazard and atmospheric effects," *Nature*, vol. 375, no. 6531, pp. 477–479, Jun. 2003.

[16] W. I. Rose, Y. Gu, I. Watson, T. Yu, G. Bluth, A. Prata, A. Krueger, N. Krotokov, S. Carn, M. Fromm, D. Hunton, A. Viggiano, T. Miller, J. Balletin, G. Ernst, J. Reeves, C. Wilson, and B. Anderson, "The February-March 2000 eruption of Hekla, Iceland, from a satellite perspective," in *Volcanism and the Earth Atmosphere, AGU Geophysical Monograph*, A. Robock and C. Oppenheimer, Eds. Washington, DC: AGU, 2003, pp. 107–132.

[17] G. C. Mayberry, W. I. Rose, and G. J. S. Bluth, "Dynamics of the volcanic and meteorological clouds produced by the December 26, 1997 eruption of Soufrire Hills Volcano, Montserrat," in *The Eruption of Soufriere Hills Volcano, Montserrat, 1995–1999*, T. Druitt and P. Kokelaar, Eds. London, U.K.: Geol. Soc. London, 2003, pp. 539–555.

[18] S. Guo, G. J. S. Bluth, W. I. Rose, I. M. Watson, and A. J. Prata, "Reevaluation of SO_2 release of the climactic June 15, 1991 Pinatubo eruption using TOMS and TOVS satellite data," *Geochem. Geophys. Geosyst.*, vol. 4, p. Q04 001, 2004, DOI: 10.1029/2003GC000654.

[19] C. Textor, H.-F. Graf, M. Herzog, J. M. Oberhuber, W. I. Rose, and G. G. J Ernst, "Volcanic particle aggregation in explosive eruption columns. Part I: Parameterization of the microphysics of hydrometeors and ash," *J. Volcanol. Geotherm. Res.*, vol. 150, no. 4, pp. 359–377, Feb. 2005.
[20] C. Textor, H.-F. Graf, M. Herzog, J. M. Oberhuber, W. I. Rose, and G. G. J Ernst, "Volcanic particle aggregation in explosive eruption columns. Part II: Numerical experiments," *J. Volcanol. Geotherm. Res.*, vol. 150, no. 4, pp. 399–394, Feb. 2005.
[21] F. S. Marzano, S. Marchiotto, S. Barbieri, D. Schneider, C. Textor, and G. Giuliani, "Ground-based radar remote sensing of explosive volcanic ash eruptions: Numerical models and quantitative applications," in *Proc. USEReST Monit. Volcanoes Seismogenic Areas*, Naples, Italy, Nov. 11–14, 2008.
[22] M. Barkat, *Signal Detection and Estimation*. Norwood, MA: Artech House, 1991.
[23] F. S. Marzano, A. Mugnai, G. Panegrossi, N. Pierdicca, E. A. Smith, and J. Turk, "Bayesian estimation of precipitating cloud parameters from combined measurements of spaceborne microwave radiometer and radar," *IEEE Trans. Geosci. Remote Sens.*, vol. 37, no. 1, pp. 596–613, Jan. 1999.
[24] F. S. Marzano, D. Scaranari, M. Montopoli, and G. Vulpiani, "Supervised classification and estimation of hydrometeors from C-band dual-polarized radars: A Bayesian approach," *IEEE Trans. Geosci. Remote Sens.*, vol. 46, no. 1, pp. 13–27, Jan. 2008.
[25] T. Petersen, S. De Angelis, G. Tytgat, and S. R. McNutt, "Local infrasound observations of large ash explosions at Augustine Volcano, Alaska during January 11–28," *Geophys. Res. Lett.*, vol. 33, no. 12, p. L12 303, Jun. 2006, DOI: 10.1029/2006GL026491.
[26] T. D. Crum, R. L. Alberty, and D. W. Burgess, "Recording, archiving, and using WSR-88D data," *Bull. Amer. Meteorol. Soc.*, vol. 74, no. 4, pp. 645–653, Apr. 1993.
[27] M. Herzog, J. M. Oberhuber, and H. Graf, "A prognostic turbulence scheme for the non-hydrostatic plume model ATHAM," *J. Atmos. Sci.*, vol. 60, no. 22, pp. 2783–2796, Nov. 2003.
[28] H.-F. Graf, M. Herzog, J. M. Oberhuber, and C. Textor, "The effect of environmental conditions on volcanic plume rise," *J. Geophys. Res.*, vol. 104, no. D20, pp. 24 309–24 320, Oct. 1999.
[29] J. M. Oberhuber, M. Herzog, H.-F. Graf, and K. Schwanke, "Volcanic plume simulation on large scales," *J. Volcanol. Geotherm. Res.*, vol. 87, no. 1–4, pp. 29–53, Dec. 1998.
[30] G. Luderer, J. Trentmann, T. Winterrath, M. O. Andreae, C. Textor, and M. Herzog, "Modeling of biomass smoke injection into the lower stratosphere by a large forest fire (Part II): Sensitivity studies," *Atmos. Chem. Phys.*, vol. 6, pp. 5261–5277, 2006.
[31] R. L. Walko, W. R. Cotton, M. P. Meyers, and J. Y. Harrington, "New RAMS cloud microphysics parameterization. Part I: The single moment scheme," *Atmos. Res.*, vol. 38, no. 1–4, pp. 29–62, Sep. 1995.
[32] M. P. Meyers, R. L. Walko, J. Y. Harrington, and W. R. Cotton, "New RAMS cloud microphysics parameterization. Part II: The two moment scheme," *Atmos. Res.*, vol. 45, no. 1, pp. 3–39, Aug. 1997.
[33] D. M. Harris and W. I. Rose, "Estimating particle sizes, concentrations and total mass of ash in volcanic clouds using weather radar," *J. Geophys. Res.*, vol. 88, no. C15, pp. 10 969–10 983, Dec. 1983.
[34] R. S. J. Sparks, M. I. Bursik, S. N. Carey, J. S. Gilbert, L. Glaze, H. Sigurdsson, and A. W. Woods, *Volcanic Plumes*. New York: Wiley, 1997.
[35] P. Willis, "Functional fits to some observed drop size distributions and parameterization of rain," *J. Atmos. Sci.*, vol. 41, no. 9, pp. 1648–1661, May 1984.
[36] H. Sauvageot, *Radar Meteorology*. Norwood, MA: Artech House, 1992.
[37] G. Mie, "Beiträge zur Optik trüber Medien, speziell kolloidaler Metallösungen," *Ann. Phys.*, vol. 25, pp. 377–445, 1908.
[38] R. L. Olsen, D. V. Rogers, and D. B. Hodge, "The *aRb* relation in the calculation of rain attenuation," *IEEE Trans. Antennas Propag.*, vol. AP-26, no. 2, pp. 318–329, Mar. 1978.
[39] C. F. Bohren and D. R. Huffman, *Absorption and Scattering of Light by Small Particles*. New York: Wiley, 1983.
[40] H. J. Liebe, G. A. Hufford, and T. Manabe, "A model for the complex permittivity of water at frequencies below 1 THz," *Int. J. Infrared Millim. Waves*, vol. 12, no. 7, pp. 659–675, Jul. 1991.
[41] R. Adams, W. F. Perger, W. I. Rose, and A. Kostinski, "Measurements of the complex dielectric constant of volcanic ash from 4 to 19 GHz," *J. Geophys. Res.*, vol. 101, no. B4, pp. 8175–8185, Apr. 1996.

Frank Silvio Marzano (S'89–M'99–SM'03) received the Laurea degree (*cum laude*) in electrical engineering and the Ph.D. degree in applied electromagnetics from the Sapienza University of Rome, Rome, Italy, in 1988 and 1993, respectively.

In 1993, he collaborated with the Institute of Atmospheric Physics, CNR, Rome. From 1994 to 1996, he was with the Italian Space Agency, Rome, as a Postdoctorate Researcher. After being a Lecturer with the University of Perugia, Perugia, Italy, in 1997, he joined the Department of Electrical Engineering and the Center of Excellence CETEMPS, University of L'Aquila, L'Aquila, Italy, as a Vice-Director and was coordinating with the Satellite and Radar Remote Sensing Laboratory. In 2005, he joined the Department of Electronic Engineering, Sapienza University of Rome, where he currently teaches courses on antennas, propagation, and remote sensing. His current research concerns passive and active remote sensing of the atmosphere from ground-based, airborne, and spaceborne platforms, with a particular focus on precipitation using microwave and infrared data, development of inversion methods, radiative transfer modeling of scattering media, and radar meteorology issues. He is also involved in radiopropagation topics in relation to incoherent wave modeling, scintillation prediction, and rain fading analysis along satellite microwave links.

Dr. Marzano received the Young Scientist Award of the XXIV URSI General Assembly in 1993. In 1998, he was the recipient of the ARPAD award from NRL Washington, DC. In 2009, he received the Best Oral Paper Award in propagation from the EuCAP Conference in Berlin. Since 2001, he has been the Italian national delegate for the European COST actions n. 720 and n. 280, ES0802, and IC0702. Since January 2004, he has been acting as an Associate Editor of the IEEE GEOSCIENCE AND REMOTE SENSING LETTERS.

Sara Marchiotto received the Laurea degree in telecommunications engineering from the Sapienza University of Rome, Rome, Italy, in 2008, with a master's thesis on radar volcanology.

Since July 2008, she has been with Altran, Rome, working on space system applications.

Christiane Textor received the Ph.D. degree from the Department of Geosciences, University of Hamburg, Hamburg, Germany, in 1999.

During and after her thesis, she worked at the Max Planck Institute for Meterology, Hamburg, focusing on numerical modeling of atmospheric processes in highly convective plumes from volcanoes and fires. In 2002, she joined the Laboratoire des Sciences du Climat et de l'Environnement, CEA-CNRS-UVSQ, Gif-sur-Yvette, France, to work with global aerosol models, focusing on aerosol processes and their radiative effects on climate. In 2006, she joined the Service d'Aeronomie, CNRS, Paris, France, continuing her research on aerosol model intercomparisons and validation. Since 2007, she has been the Scientific Coordinator of the GEOmon project, dealing with *in situ* observations of atmospheric tracers in order to establish recent trends. She is currently with the Deutsche IPCC-Koordinierungsstelle–Projektträger im DLR Umwelt, Kultur, Nachhaltigkeit Heinrich-Konen-Str.1–53227 Bonn, Germany. Her research focuses on aerosol processes in the atmosphere on a small scale (volcanic eruption column) and on a large scale (global climate effects).

David J. Schneider received the Ph.D. degree in geology and volcanology from the Michigan Technological University, Houghton, in 2000.

Since 1997, he has been a Research Geophysicist with the Alaska Volcano Observatory, U.S. Geological Survey, Anchorage, AK. His area of specialization is the research and monitoring of volcanic activity using remote sensing. His interests include satellite measurements of ash and sulfur dioxide, ground-based and airborne thermal imaging, and ground-based radar observations of ash emissions.